On/off Switchable Epicatechin-based ultra-sensitive MRI visible nanotheranostics – See it and treat it

Bing Xiao, [a, c, †] Xiaoxuan Zhou, [b, †] Hongxia Xu, [a] Wei Zhang, [a] Xiaodan Xu, [a] Fengjuan Tian, [b] Yue Qian, [b] Feidan Yu, [b] Cailing Pu, [b] Hongjie Hu, [b]* Zhuxian Zhou, [a] Xiangrui Liu, [a] Hirak K Patra, [d]* Nigel Slater, [d] Jianbin Tang, [a]* Jianqing Gao [c], Youqing Shen [a]

ABSTRACT:

Nanotechnology has a remarkable impact on preclinical development for future medicines. However, the complicated preparation and systemic toxicity in the living system render them from clinical translations. In the present report, we have developed an polyepicatechin-based on/off switchable ultra-sensitive magnetic resonance imaging (MRI) visible nanotheranostic nanoparticle (PEMN) for image-guided photothermal therapy (PTT) using our strategy of integrating polymerization and biomineralization in protein template. We have exploited natural polyphenols as the near infra-red (NIR) switchable photothermal source and MnO_2 for MRI-guided theranostics. PEMN demonstrates excellent MRI contrast ability with longitudinal relaxivity value up to

---

[a] *Key Laboratory of Biomass Chemical Engineering of Ministry of Education, Center for Bionanoengineering, and College of Chemical and Biological Engineering, Zhejiang University, Hangzhou, Zhejiang, 310027, China.*

[b] *Department of Radiology, Sir Run Run Shaw Hospital (SRRSH) of School of Medicine, Zhejiang University, Hangzhou, Zhejiang, 310016, China.*

[c] *College of Pharmaceutical Sciences, Zhejiang University, Hangzhou 310058, China*

[d] *Department of Chemical Engineering and Biotechnology, University of Cambridge, Cambridge, United Kingdom*

* Corresponding Author: hongjiehu@zju.edu.cn; hp401@cam.ac.uk; jianbin@zju.edu.cn；

†These authors equally contributed to this work.

30.01 mM^{-1}s^{-1}. PEMN has shown great tumor inhibition on orthotopic breast tumors and the treatment could be made switchable with on/off interchangeable mode as per requirement. PEMN was found excretable mainly through kidneys, avoiding potential systemic toxicity. Thus, PEMN could be extremely useful for developing on-demand therapeutics via 'see it and treat it' means with distinguished MRI capability and on/off switchable photothermal property.

Introduction

The World Health Organisation (WHO) recently made a resolution on 'Cancer Prevention and Control through an Integrated Approach' and is looking for immediate better and alternative strategies through setting up Global Action Plan with UN Agenda 2030 to reduce cancer-associated mortality[1]. The current ongoing therapeutic lines are well known with their associated side effects at times up to the level that causing myth whether cancer treatment is worse than cancer itself.[2] Thousands of chemical and biological agents are showing their potential as anti-cancer drug candidates but unfortunately not being translated into clinics for their collateral damages and extreme side effects[3]. The key challenge fundamentally remains the same to develop physiologically safer and technically tractable therapy. Therefore, there are increasing demands for better control on all three major existing anti-cancer strategies (surgery, chemotherapy and radiation). In this regard, the nanotechnology-based approaches are rapidly emerging with pre-clinical successes as future advanced cancer therapeutics.[4]

Photothermal therapy (PTT) and induced hyperthermia based strategies are already stood out as a well-controlled safer therapeutic scheme in many clinical trials[5]. Nanotechnology assisting photo-induced hyperthermia is evolving as one of the major non-chemotherapeutic noninvasive treatment strategies of various malignancies including metastasis[6]. For example, NanoTherm® is one such novel strategy already approved in Europe to treat glioblastoma by inducing hyperthermia non-invasively.[7-9]

Moreover, the emergence of competent photothermal candidates with defined imaging alignment can significantly enrich the curative effect by allowing real-time screening of the therapeutic progress. Up till now, numerous nano and microscale

organic and inorganic materials including conjugated polymers[10-13], carbon nanotubes[14-17] and metallic oxides[18-21] had been investigated for PTT of cancers. Among them, polymers including polydopamine[22-24], polypyrrole[25-27] and polyaniline[28-32], synthesized via oxidation polymerization of their respective monomers, have shown excellent potential in PTT. Later on, especially, polydopamine is widely explored in integration of PTT for biological imaging[24], gene therapy[33], chemotherapy[22] and photodynamic therapy (PDT)[34] due to their simple preparation, easy functionalization, strong metallic ion co-ordination, excellent thermal conversion efficiency and good biocompatibility. However, further functionalization and polydopamine-derived nanotheranostic agents have found to be compromised for their less biocompatibility, leading to high risks of being translated.

In comparison with polyamines, polyphenols are less explored but can also be polymerized using small polyphenol monomers (e.g., epicatechin and tannin). Such polymers have the potential to play vital roles in photothermal-related multifunctional nanosystems as stabilizers, surfactants or reagents.[35-38] Recently, Bai et al., has applied polycatechol innovatively as an operative nanocarrier for chemo-photothermal dual therapy.[39] In another example, dendritic polyphenol recently explored as a polydentate ligand to establish a novel multipurpose PTT platform.[40] One such multifunctional nanoparticles (FeAP-NPs) developed using fruit-extracted natural polyphenols (ACN) were reported with selective tumor accumulation, lower level of toxicity and rapid renal clearance.[41]

However, the MRI and PTT properties as well as the biocompatibility of these limitedly reported polyphenols could not satisfy the requirements for clinical application. Our group has recently developed an integrated polymerization-biomineralization method for developing multifunctional nanotheranostic strategies[23]. But establishing polyphenol-derived agents with first-rate multifunctional efficiency with low toxicity remains challenging. Herein, we have exploited a multifunctional nanotheranostic platform polyepicatechin-MnO$_2$ nanoparticle (PEMN) using natural flavonoid epicatechin[42]. We have exploited this natural molecule to develop on/off switchable PTT platform integrated with MnO$_2$ for ultra-sensitive MRI visibility.

PEMN demonstrated its distinguished potential for prospective MRI-guided PTT, including the capability of detection of metastasized tumors while the tool itself is biocompatible and easily excretable (high kidney clearance rate).

Results and discussion

Synthesis and characterization of PEMN

We have synthesized PEMN with the modification of our recently established one-step integration of polymerization and biomineralization strategy at mild temperature.[23] In brief, $KMnO_4$ (0.19 µmol) was used in a mixture of aqueous protein (BSA, 1.51×10^{-3} µmol) and epicatechin monomer solution (0.34 µmol) and then magnetic stirred at room temperature. During the process, epicatechin monomers polymerized under the oxidation of $KMnO_4$ and the formed MnO_2 mineralized into hybrid nanoparticles in the BSA template. Dynamic laser scattering (DLS) shown the average hydrodynamic diameters (H_D) of PEMN modules were 37 nm (**Figure 1a**), which was also indicated by transmission electron microscopy (TEM).

The X-ray photoelectron spectroscopy (XPS) spectra of PEMN showed two classic binding-energy peaks at 642.5 eV and 654.0 eV, corresponding to Mn (IV)$_{2p3/2}$ and Mn (IV)$_{2p1/2}$ respectively (**Figure 1b**). X-ray diffraction (XRD) patterns confirmed that PEMN contains MnO_2 (**Figure 1c**). The Mn content in PEMN was 2.56% which was further confirmed under Inductively coupled plasma-mass spectroscopy (ICP-MS). The circular dichroism (CD) spectra reflected that PEMN existed the secondary structure of the protein used after oxidating by $KMnO_4$ (**Figure 1d**), and the FT-IR spectrum of PEMN showed the BSA and PEG typical peaks (**Figure 1e**). More importantly, similar to natural epicatechin monomer, PEMN showed a strong and sharp band at around 1638 cm^{-1} in Raman spectrum reflecting the vibration peak of carbon atom sp^2 on the benzene ring from the polyphenolic component present in PEMN (**Figure 1f**).[43-45] The elemental profile mapping of PEMN together with energy dispersive spectrometry (EDS) and XPS spectrum also identified the evidence of C, O, N, and Mn elements in the PEMN (**Figure 1g, Figure S1**). Taken together, the in-

detailed characterizations suggest that PEMN comprised of polyphenols and protein hybrid matrix with scattering spherical MnO_2 inside. The obtained zeta potential of -16.7 mV in PEMN solution had no significant variation and PEMN also showed high stability in different mediums including phosphate buffer solution (PBS), deionized water, normal saline, complete medium, and serum only (**Figure S2**). We also found no remarkable Mn ions leakage within seven days (**Figure S3**). PEMN solution showed high stability mainly own to the coinstantaneous restriction of the MnO_2 by both polyphenols and the protein BSA.

PEMN solution showed remarkable growth in temperature under exposure by 808 nm laser with the increasing concentration of Mn, while there was no observable increase in temperature for water under the same irradiation condition, suggesting PEMN could serve as a favorable PTT (**Figure 2a**) of the biological tissue. According to the data from **Figure 2b and 2c,** compared with polydopamine (ca. 40%) or polypyrrole (ca. 26%) from previous reports, PEMN exhibited higher photothermal conversion efficiency (η, 41.5%).[46, 47] The excellent η value of PEMN benefited from the intense NIR spectrum absorption (808 nm) as well as the highly electron-transfer efficiency by manganese (**Figure S4**).[48, 49] Furthermore, PEMN showed good photothermal stability along with recycling the temperature alterations (**Figure 2d**), indicating that the PTT with PEMN was on/off switchable through turning on/off laser irradiation. Importantly, there were no changes in relaxation time with or without laser irradiation and hydrodynamic diameter of PEMN for seven days (**Figure S2d**), confirming the feasibility of application and outstanding photothermal capability of the developed PEMN. Above all, PEMN was a promising platform for switchable theranostics considering its outstanding photothermal stability, photothermal transfer efficiency, and switchable properties.

Cytotoxicity of PEMN

The regular MTT assay revealed the cytotoxicity of PEMN with/without laser irradiation. The cells incubated with PEMN alone indicated a negligible influence on cell viability. Conversely, 4T1 murine breast tumor cells treated with PEMN and laser

exposure showed obvious cell toxicity (**Figure 2e**). These results were reconfirmed by co-incubation with PI/Calcein-AM under a confocal laser scanning microscopy (CLSM) (**Figure 2f**). The tumor cells incubated with PEMN plus laser exposure led to cellular death, while those without laser irradiation were still alive, verifying excellent hyperthermia mediated cell killing effect and high safety of PEMN. The cytotoxicity of PEMN with/without laser irradiation was studied by AnnexinV-FITC/PI double staining assay. PEMN with laser irradiation could induce tumor cell apoptosis (Figure S5).

MRI performance

PEMN was supposed to be a potential T_1-weight MRI contrast agent. The curve of PEMN concentration-dependent relaxation rate ($1/T_1$) showed longitudinal relaxivity (r_1) values (**Figure 3a**). The r_1 values of PEMN were calculated to be 30.01 $mM^{-1}s^{-1}$, about 6.9 times higher than that for the clinically used Gd-DTPA[50] and also higher than other reported manganese-derived nanotheranostic compounds.[51-54] It was probably because MnO_2 particles of PEMN were both restricted by BSA and polyepicatechin, which led to more rigid structure and thereby a longer rotational tumbling time (τ_R).[55] The brighter MR images displayed with the increase of Mn concentration (**Figure 3b**). PEMN with super high r_1 value made it a favorable MRI contrast agent for tumor detection and differentiation.

The MRI performance of PEMN *in vivo* was further examined. 4T1 orthotopic tumor-bearing female Balb/c mice model was constructed, followed by injecting with PEMN solution intravenously (56 μmol kg^{-1} Mn). MR images was obtained at different time points using a 3T MR clinical system (**Figure 3c**). The tumor was delineated by a hyper-enhanced rim contrasted by PEMN in 5 min, following centripetal fill-in enhancement of the whole tumor site lasting for at least two hours. This provided precise differentiation between cancerous lesions and other normal tissues. The tumor signal changes were quantitatively calculated, showing T_1-weighted signal enhancement of 68% at 30 min post-injection (**Figure 3f**).

After injection of PEMN at a low dosage (28 μmol Kg^{-1} Mn), PEMN was observed partially to be metabolized through the urinary and hepatobiliary system of healthy

mice (**Figure S6**). As shown in **Figure 3e**, the kidneys were gradually enhanced by PEMN in 5 min and lasted for at least two hours, providing precise differentiation between renal parenchyma and pelvis. Meanwhile, the renal pyramid and column in the medulla and the cortex could be well distinguished within five minutes to half an hour after administration, showing renal enhancement superiority compared with our previous report[23]. To test whether PEMN could enable detection of metastasized tumors, the mice bearing intrahepatic metastases were injected PEMN (56 μmol kg^{-1} Mn). The pre-scanning T_1-weighted image showed no difference between the metastatic lesions and normal liver tissues. By contrast, the metastatic niches under the liver background showed hyperintense after the treatment of PEMN, which were clearly distinguished at 1 h after injection (**Figure 3d and Figure 3g**). The liver with metastases was further dissected and confirmed by histological and pathological staining (**Figure S7**).

In vivo PTT of PEMN

The tumor inhibition ability of PEMN was tested with the 4T1 orthotopic breast cancer mice model. The mice received single-injection of PEMN (28 μmol Kg^{-1} Mn), and then 808 nm laser exposure (2 W cm^{-2}, 5 min) was performed at 30 min post-injection. The ideal time window was indicated by the MRI through the 'see it and treat it' mode, which revealed that the maximum tumor accumulation of PEMN was 30 min post-injection. Meanwhile, an infrared camera was used to monitor the temperature variation in the tumors during laser irradiation. The surface temperature of the tumor in the PEMN-treated group with laser irradiation drastically increased up to 50 ℃, whereas that in the PBS-treated group barely increased (**Figure 4a** and **Figure 4b**). As a consequence, the three groups with the treatment of PBS, only laser irradiation, or PEMN alone without laser irradiation showed rapid tumor growth. In contrast, the group with both treatment of PEMN and laser exposure revealed efficient inhibition capacity on tumor growth without recurrence (**Figure 4c and Figure S8a**). Furthermore, all the mice were observed no noticeable weight loss, revealing low side effects (**Figure S8b**). Remarkably, the group with PEMN treatment and laser exposure showed

complete tumor ablation and survived during follow-up of 60 days, whereas the other group treated with PEMN only, laser only and PBS survived for less than 36 days. Noteworthily, as the PTT with PEMN was on/off switchable and was localized in tumor, the damage to other organs could be avoided. As shown in Figure 4d, like the major organs from healthy blank mice, the slices with H&E-staining from the group with PEMN treatment and laser exposure demonstrated no noticeable injuries or necrosis (**Figure 4d**). These results illustrated that PEMN could be a promising photothermal cancer therapy agent.

Biosafety and biodistribution

A biosafety study was performed to testify its potential as a nanotheranostic agent for clinical translation *in vivo*. Sprague Dawley (SD) rats administrated with PEMN twice of the therapeutic dosage (56 µmol kg^{-1} Mn) remained healthy and showed steady body weight growth for 30 days (**Figure 5c**). Compared with the untreated group, the serum biochemistry and complete blood profile of the PEMN-treated rats were carefully collected and analyzed. **Figure 5d** showed no obvious differences in blood routine, liver function and kidney function parameters were observed between the PEMN-treated and control groups, implying that PEMN had no noticeable poisonous renal and hepatic side effects. Next, the pathological analysis of the major organs from the PEMN-treated mice indicated no obvious tissue damage or inflammatory changes 60 days after intravenous injection of PEMN (28 µmol kg^{-1} Mn) (**Figure S9**). All these data confirmed that PEMN had excellent biocompatibility and biosafety for *in vivo* application.

For blood circulation study, the content of Mn was analyzed at various time points after PEMN treatment (56 µmol kg^{-1} Mn). The blood circulation half-life of PEMN was about 5.4 h (**Figure 5a**), showing that PEMN could be initially accumulated in the tumors for theranostics during the period of observation and then be cleared over time. According to the time-dependent biodistribution curve, the tumor accumulation of PEMN was about 6.0 % ID g^{-1} 1 day after injection, which would be favorable for PTT agent (**Figure 5b**). Moreover, manganese was nearly completely excreted in 7 days

after injection mainly through kidneys and liver, which was concordant with the coronal T_1-weighted MR images (**Figure S5**). Additionally, the urine and feces of the PEMN-treated mice (56 μmol kg^{-1} Mn) were collected at various time points and analyzed using the ICP-MS. A major portion of PEMN (28.6% ID^{-1}) was excreted by the urinary system into urine at 12 h post-injection, and a small portion (8.9% ID g^{-1}) was cleared by the digestive tract in the feces (**Figure S10**). Above all, PEMN exhibited efficient renal clearance, and correspondently weakened the risk of hepatic toxicity, which is one of the main obstacles limiting the clinical application of nanotheranostics.

Conclusions

In summary, a nanotheranostic PEMN platform was developed that can be efficiently synthesized and easily convertible for industrial–scale formulation employing one-pot integrated biomineralization-polymerization method. PEMN exhibited high r$_1$s (30.01 mM^{-1}s^{-1}) for helping orthotopic breast cancer and liver metastases detection and also outstanding photothermal transfer efficiency (41.5%) for treating the tumors. The excellent switchable properties of PEMN can allow the clinician to *see it and treat it* options. Thus, if PEMN is found on the off-target site, one can easily avoid the PTT and allow the module to rapidly excrete from the body without collateral damages to the other organs. PTT eliminated orthotopic breast tumors completely without significant toxic side effects after treatment. A nanotheranostic agent PEMN with excellent biocompatibility, illustrious imaging plus efficient PTT performance has enormous potential in MRI-guided PTT.

Experimental section

Materials

Epigallocatechin (EGC) was obtained from Shanghai Tansoole Co., Ltd. China. Potassium permanganate (KMnO$_4$) was acquired from Shanghai Sinopharm Chemical Reagent Co., Ltd. China. Bovine serum albumin (BSA) was purchased from Shanghai Sangon Biotech Co., Ltd. China. Fetal bovine serum (FBS) was obtained from AG

Gibco Life Technologies, Switzerland. RPMI-1640 medium was purchased from GE Healthcare Co., Ltd. 3-(4, 5-dimethylthiazol-2-yl)-2, 5-diphenyltetrazolium bromide (MTT) was obtained from Sigma-Aldrich.

Synthetic method

The theranostic nanoparticles were synthesized through one-step combination of polymerization and biomineralization at a mild temperature according to our previous report[23]. In brief, epicatechin monomer (0.34 μmol) and equivalent BSA (1.51×10^{-3} μmol) were mixed in deionized water (98 mL). $KMnO_4$ (0.19 μmol) dissolved in deionized water (2 mL) was dropped into the mixture in 5 min, and then the prepared solution was magnetically stirred at ambient temperature for 4 h. Finally, the obtained colloidal was purified through dialysis (cut-off MW 8-14 kDa) against water to remove excess precursors, and then mixed with PEG-NH2 (MW 5000). The polyepicatechin-MnO_2 nanoparticle (PEMN) was obtained after ultrafiltration.

Characterization.

The particle dispersion index (PDI), ζ-potential and hydrodynamic size distribution of PEMN nanoparticle were recorded by the dynamic light scattering instrument (DLS, Nano ZS, Malvern). The morphology of PEMN nanoparticles were characterized under the transmission electron microscopy (TEM, JEM-1230). Element maps, as well as the results of EDS scanning, were obtained on a field-emission scanning electron microscope (FESEM, SU-8010, Hitachi, Japan). The UV−visible absorption spectra and OD values were obtained on a SpectraMax M2^e Microplate Reader. The CD spectra of protein BSA and PEMN were recorded using a spectropolarimeter system (JASCO, J-1500-150ST). The XPS results were obtained using an ESCALAB 250Xi (Thermo Scientific) with the radiation from an Al Kα (1486.6 eV) X-ray source. The Mn concentration in the PEMN solution was tested on the inductively coupled plasma-mass spectroscopy (ICP-MS, PerkinElmer). The Mn released from PEMN was studied in aqueous solution. The fourier transform infrared (FT-IR) spectra (4000-400 cm^{-1}) was recorded using a Magna-560 spectrometer (Nicolet, iS50, USA). The longitudinal relaxivities were measured by a 0.52-T MicroMR Analyzer (Shanghai Niumag Corporation, China). The confocal images were taken by a Nikon A1 confocal laser

scanning microscopy. MR images involving tube samples and mice were operated on a clinical 3T MRI scanner (Discovery 750w 3T, GE Healthcare, Waukesha, WI, USA) equipped with a mice coil.

In vivo PTT

For in vitro photothermal experiment, the nanoparticles PEMN solution with different concentrations of Mn (0.175, 0.35, 0.7, 1.4 and 2.8 mM) in a centrifuge tube under the same irradiation condition (808 nm, 2 W cm^{-2}, 5 min), and then recorded the temperature changes every 10 seconds by a photothermal imager. Besides, with NIR laser on and off, the temperature variation was also rrecored and then calculated photothermal conversion efficiency (η). In addition, temperature change of PEMN under four laser irradiation on/off cycles was recored.

4.5 Cellular Experiments

The standard MTT (3-(4, 5-dimethylthiazol-2-yl)-2, 5-diphenyltetrazolium bromide) experiments were applied to study the cytotoxicity of PEMN. The murine mammary tumor cells line 4T1 were incubated with PEMN only or PMEN-treated plus laser irradiation (808 nm, 2 W cm^{-2}, 5 min) at predesigned concentrations (6.25, 12.5, 25, 50, 100, 200, 400, 500 µM Mn). For the confocal imaging of propidium iodide/calcein acetoxymethyl ester (PI/Calcein-AM) co-staining, PEMN (100 µM Mn) was incubated with 4T1 cells in glass bottom for 30 min, and then treated with 808 nm laser irradiation for 5 min. The cytotoxicity of PEMN with/without laser irradiation was studied by flow cytometry analysis with AnnexinV-FITC/PI double staining.

Colloidal and optical stability measurement

For direct observation of colloidal stability, PEMN solutions were dispersed in DI water, PBS (10 mM, pH=7.4), RPMI-1640 culture medium, FBS, and normal saline, respectively. The photos were taken to monitor the colloidal stability in 15 days. For visualization of photostability, the PEMN (2 mg mL^{-1}) were respectively mixed with DI water, PBS (pH 7.4), normal saline, or RMPI-1640 with 10% fetal bovine serum. Subsequently, the UV-vis absorption and Hydrodynamic diameters (HD) were monitored throughout a period of 7 days. Moreover, the changes in longitudinal relaxation times (T$_1$) of the PEMNpre- and post- laser exposure were also recorded.

Tumor Models

Institutional Ethical Committee of Animal Experimentation of Zhejiang University in China allowed the animal studies in this study, and the guidelines from the Experimental Animals Institute of Zhejiang University were strictly obeyed. The Sprague Dawley (SD) rats and Balb/c female mice were purchased from Shanghai Silaike Jingda Co., Ltd., China. For the orthotopic 4T1 tumor model, 5×10^5 cells in PBS (200 μL) were injected into the right third mammary gland of the mice, and all the corresponding experiments were performed as the tumor volume grew up to 60 mm^3. For the liver metastasis mice model, 40 μL PBS containing 10×10^5 4T1 cells was injected into the parenchyma of the spleen, following splenectomy after 5 min, and then performed the abdominal closure.

MR Imaging

For *in vitro* imaging through MR scanner, PEMN with various concentrations (0.05-0.2 mM) was stored in a 0.6 ml centrifuge tube and scanned under a 0.52-T MicroMR Imaging & Analyzer at room temperature. For imaging of the orthotopic 4T1 breast tumor mice model, the mice were administrated with PEMN (i.v. 56 μmol Kg^{-1} Mn). For imaging of liver metastases mice model, the abdominal MR images were taken on the 12th day after injecting 4T1 cells. For MR imaging of kidneys, 28 μmol Kg^{-1} Mn of PEMN solution was intravenously injected into normal mice. All the images were collected at predetermined timed intervals, and then signal intensities were measured and calculated. Scanning sequence of FSPGR T1-weight imaging were set as follows: time to echo / repetition time = 12/550 ms, field of view = 60×60 mm^2, slice thickness = 1 mm, number of excitations = 3, matrix size = 320×192, scanning time = 2 min and 18 sec.

In Vivo PTT

The orthotopic 4T1 breast tumor mice were randomly allocated into 4 groups (n = 5, each group): (a) PBS treated, (b) NIR laser treated (808 nm, 2 W cm^{-2}, 5 min), (c) PEMN treated (28 μmol Kg^{-1} Mn), and (d) PEMN with NIR laser treated. During 808 nm laser exposure, the changes in tumor temperature were monitored under an IR thermal imaging camera. Meanwhile, the tumor sizes were measured every alternate

day to estimate the therapeutic effect and calculated (Volume= length×wideth^2/2). The body weight was also monitored in parallel. After a follow-up of 60 days, the group treated with PEMN plus laser exposure were performed for euthanasia, and then organs and tumors were harvested and studied with H&E (Beyotime, Shanghai, China) staining.

Biosafety and Biodistribution

The SD rats (n = 3, each group) were injected with PEMN (56 μmol Kg^{-1} Mn) from the tail vein or without any treatment, and weighed every two days. For routine blood tests and blood biochemistry analysis, blood samples were obtained from the rats at 1 and 30 days. For blood circulation of PEMN, samples from normal mice (n=3) were collected at identical time points after injection PEMN (56 μmol Kg^{-1} Mn), and then quantified the Mn content by ICP-MS. For the biodistribution of PEMN, the corresponding organs, tumors, urine and feces from tumor-bearing mice (n=3) were harvested at specified time points after intravenous injection (56 μmol Kg^{-1} Mn), and then the Mn concentration was measured by ICP-MS.

Histological Assessment

The harvested organs (liver, kidney, spleen, heart, lung, and intestine) were fixed with 4% paraformaldehyde solution and embedded into paraffin. The slices of above organs were stained with H&E (Beyotime, Shanghai, China) and observed under an optical microscope (BX51, Olympus, Tokyo, Japan).

Statistical analysis

Statistical analysis was conducted using a Student's t-test. A statistically significant difference was estimated at *$p < 0.05$, **$p < 0.01$, ***$p < 0.001$. The values were expressed as the mean ± SD, as illustrated in the figure legends.
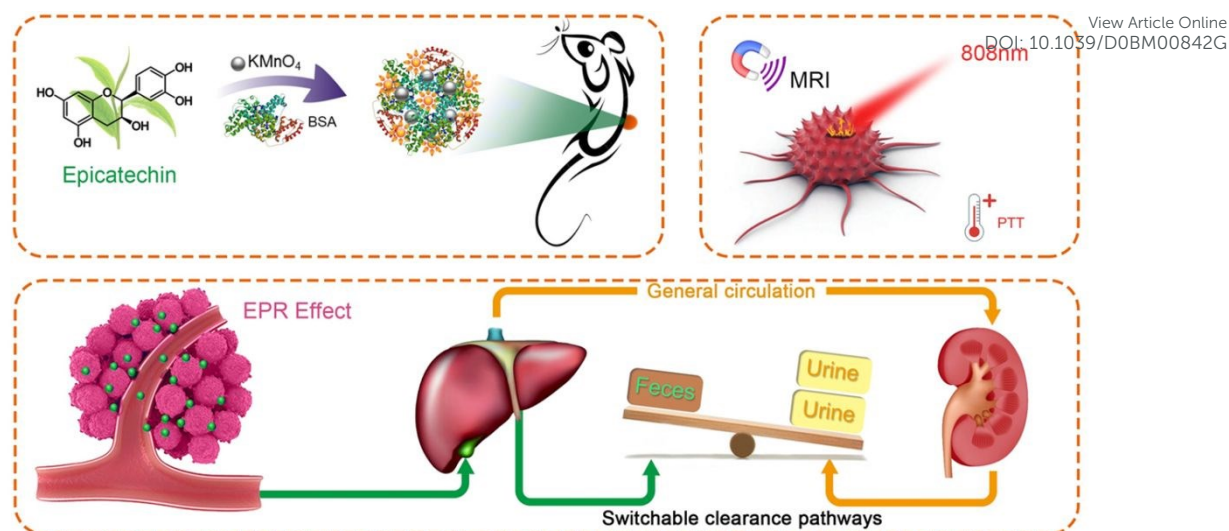
Scheme 1. Schematic illustration of novel polyphenol/MnO$_2$ hybrid theranostic agents for multifunctional MRI and photothermal therapy (PTT) *in vivo*.
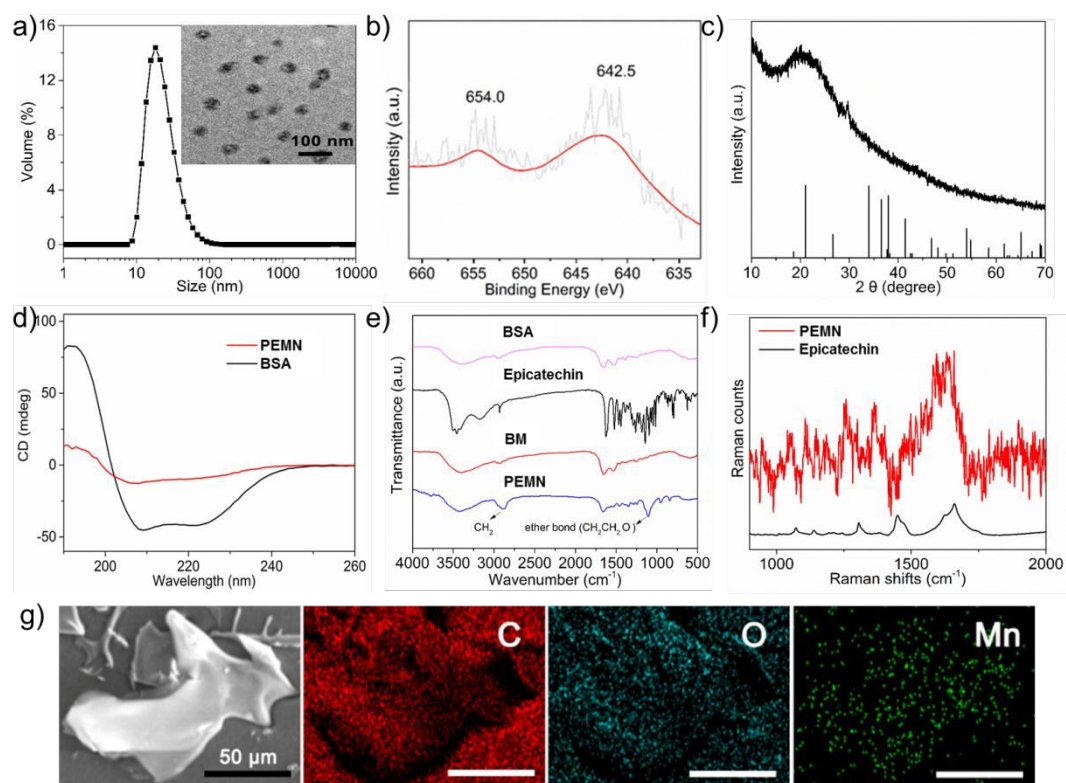

Figure 1. (a) Size distribution and (inset) TEM image of PEMN. (b) XPS spectrum of MnO$_2$ in PEMN. (c) XRD spectrum of PEMN. (d) CD spectra of pure BSA and PEMN. (e) FT-IR spectra of pure BSA, Epicatechin, and as-made PEMN. (f) Raman spectrum of PEMN. (g) FETEM image and elemental mapping images (C, O, and Mn) of PEMN.
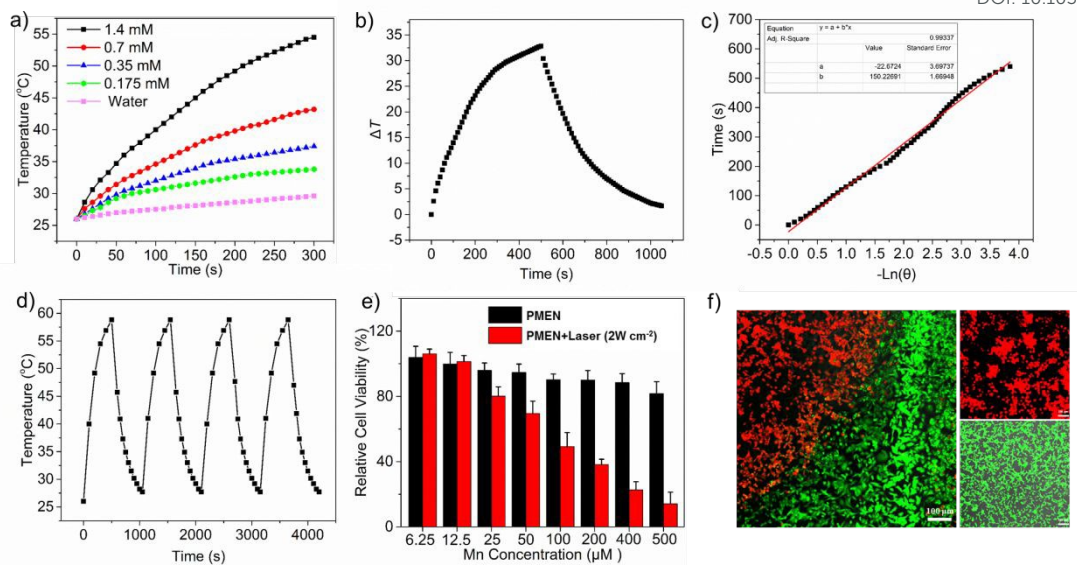
Figure 2. (a) Photothermal temperature curves of PEMN plus laser irradiation at different Mn concentration. (b) Temperature variation of PEMN with NIR laser on and off. (c) Linear time data versus $-\ln\theta$ obtained from the cooling process of (b). (d) Temperature change of PEMN under four laser irradiation on/off cycles. (e) Cell toxicity of PEMN alone or PEMN-induced PTT. (f) Confocal images of PI/Calcein-AM costained cells incubation with PEMN alone or PEMN-induced PTT for 5 min (100 µM Mn, 808 nm, 2 W cm^{-2}).
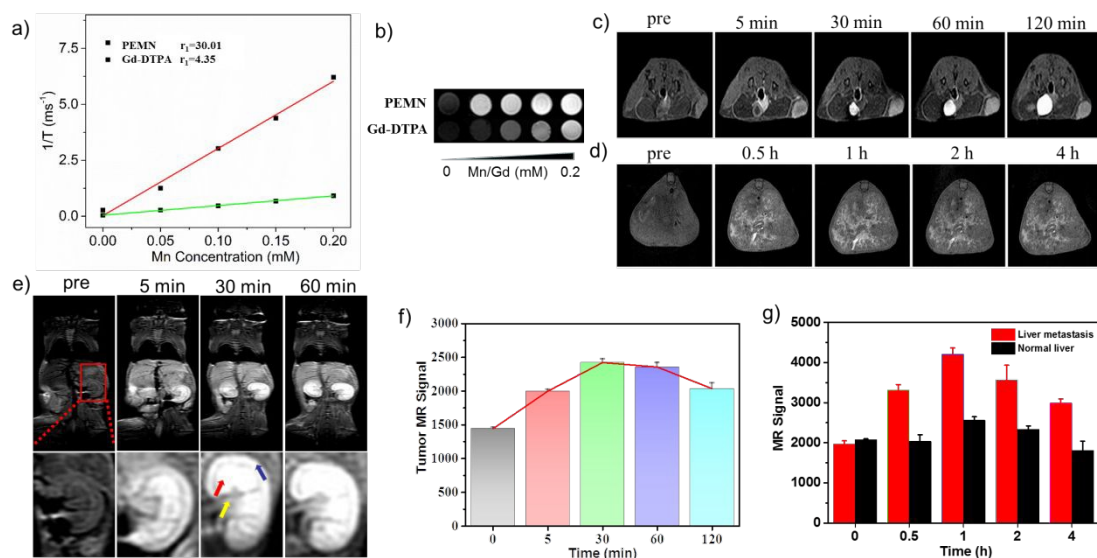

Figure 3. MRI study. (a) Relaxation rate curve of PEMN and Gd-DTPA with various Mn concentrations. (b) T$_1$-weight images of PEMN solution (upper) or Gd-DTPA

(lower) with different Mn concentrations. (c) Axial TIWIs and (f) Signal counts of 4T1 breast tumor after PEMN injection (i.v. 56 μmol Kg^{-1} Mn). (d) Abdominal TIWIs and (g) Signal intensity changes between liver metastasis sites and normal hepatic tissue after PEMN injection (i.v. 56 μmol Kg^{-1} Mn). (e) Coronal TIWIs of the whole body and kidney level (below) in the normal mice after injection of PEMN (i.v. 28 μmol Kg^{-1} Mn). The blue arrow was cortex, the red arrow was medulla, and the yellow arrow was pelvis.
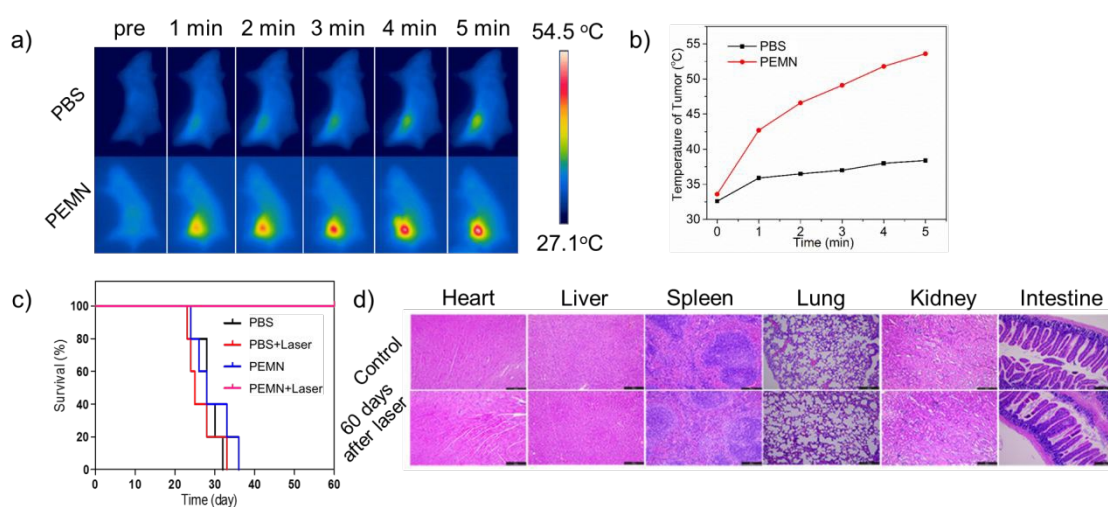

Figure 4. Photothermal therapy study on 4T1 tumor bearing mice. (a) Infrared thermal images and (b) Temperature changes of tumor sites during laser irradiation after PBS or PEMN injection. (c) Mice survival curves with different treatments (n=5). (d) H&E staining analysis between the healthy control mice and these treated with PTT of PEMN after 60 days (28 μmol Kg^{-1} Mn). Scale bar: 100 μm.
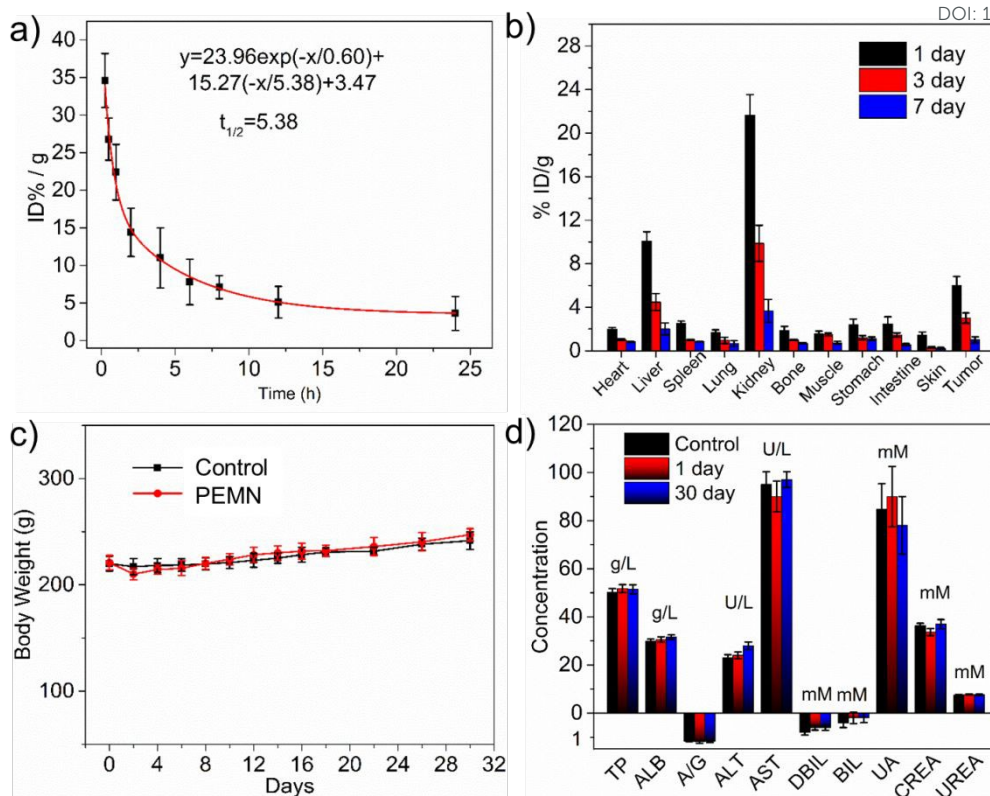
Figure 5. (a) Blood circulation profile of PEMN. (b) Time-dependent biodistribution. (c) Body weight changes and (d) Blood biochemical data of Sprague-Dawley (SD) rats with and without intravenous of PEMN versus time. (intravenous injection dosage: 56 μmol Kg^{-1} Mn). Liver function parameters (total protein, TP; alanine aminotransferase, ALT; albumin, ALB; alkaline phosphatase, ALP, and aspartate aminotransferase, AST), kidney function parameters (creatinine, CREA; urea nitrogen, UREA, and uric acid, UA).

Conflicts of interest

There are no conflicts to declare.

ACKNOWLEDGEMENTS

Biomaterials Science Accepted Manuscript

REFERENCES

1. Cancer, https://www.who.int/news-room/fact-sheets/detail/cancer).

2. C. Fletcher, C. Wilson, A. D. Hutchinson and E. A. Grunfeld, *Cancer Treat Rev*, 2018, **68**, 86-93.

3. J. I. Hare, T. Lammers, M. B. Ashford, S. Puri, G. Storm and S. T. Barry, *Adv Drug Deliv Rev*, 2017, **108**, 25-38.

4. J. Shi, P. W. Kantoff, R. Wooster and O. C. Farokhzad, *Nat Rev Cancer*, 2017, **17**, 20-37.

5. W. L. Bi, A. Hosny, M. B. Schabath, M. L. Giger, N. J. Birkbak, A. Mehrtash, T. Allison, O. Arnaout, C. Abbosh, I. F. Dunn, R. H. Mak, R. M. Tamimi, C. M. Tempany, C. Swanton, U. Hoffmann, L. H. Schwartz, R. J. Gillies, R. Y. Huang and H. Aerts, *CA Cancer J Clin*, 2019, **69**, 127.

6. D. Banerjee, A. Cieslar-Pobuda, G. H. Zhu, E. Wiechec and H. K. Patra, *Trends Pharmacol Sci*, 2019, **40**, 403-418.

7. K. Maier-Hauff, F. Ulrich, D. Nestler, H. Niehoff, P. Wust, B. Thiesen, H. Orawa, V. Budach and A. Jordan, *J Neurooncol*, 2011, **103**, 317-324.

8. E. Alphandery, P. Grand-Dewyse, R. Lefevre, C. Mandawala and M. Durand-Dubief, *Expert Rev Anticancer Ther*, 2015, **15**, 1233-1255.

9. K. Mahmoudi, A. Bouras, D. Bozec, R. Ivkov and C. Hadjipanayis, *Int J Hyperthermia*, 2018, **34**, 1316-1328.

10. P. Chen, Y. Ma, Z. Zheng, C. Wu, Y. Wang and G. Liang, *Nat Commun*, 2019, **10**, 1192.

11. J. Wang, C. Zhu, J. Han, N. Han, J. Xi, L. Fan and R. Guo, *ACS Appl Mater Inter*, 2018, **10**, 12323-12330.

12. Z. Wang, B. Guo, E. Middha, Z. Huang, Q. Hu, Z. Fu and B. Liu, *ACS Appl Mater Inter*, 2019, **11**, 11167-11176.

13. Y. Wang, S. Li, P. Zhang, H. Bai, L. Feng, F. Lv, L. Liu and S. Wang, *Adv Mater*, 2018, **30**, 1705418.

14. Q. Fu, R. Zhu, J. Song, H. Yang and X. Chen, *Adv Mater*, 2019, **31**, e1805875.

15. Q. Jia, J. Ge, W. Liu, X. Zheng, S. Chen, Y. Wen, H. Zhang and P. Wang, *Adv Mater*, 2018, **30**, e1706090.

16. L. Lin, L. Liu, B. Zhao, R. Xie, W. Lin, H. Li, Y. Li, M. Shi, Y. G. Chen, T. A. Springer and X. Chen, *Nat Nanotechnol*, 2015, **10**, 465-471.

17. B. Guo, Z. Sheng, D. Hu, C. Liu, H. Zheng and B. Liu, *Adv Mater*, 2018, **30**, e1802591.

18. L. Cheng, J. Liu, X. Gu, H. Gong, X. Shi, T. Liu, C. Wang, X. Wang, G. Liu, H. Xing, W. Bu, B. Sun and Z. Liu, *Adv Mater*, 2014, **26**, 1886-1893.

19. V. Yadav, S. Roy, P. Singh, Z. Khan and A. Jaiswal, *Small*, 2019, **15**, e1803706.

20. X. Zhu, X. Ji, N. Kong, Y. Chen, M. Mahmoudi, X. Xu, L. Ding, W. Tao, T. Cai, Y. Li, T. Gan, A. Barrett, Z. Bharwani, H. Chen and O. C. Farokhzad, *ACS Nano*, 2018, **12**, 2922-2938.

21. T. Liu, C. Wang, X. Gu, H. Gong, L. Cheng, X. Shi, L. Feng, B. Sun and Z. Liu, *Adv Mater*, 2014, **26**, 3433-3440.

22. J. Nam, S. Son, L. J. Ochyl, R. Kuai, A. Schwendeman and J. J. Moon, *Nat Commun*, 2018, **9**, 1074.

23. B. Xiao, X. Zhou, H. Xu, B. Wu, D. Hu, H. Hu, K. Pu, Z. Zhou, X. Liu, J. Tang and Y. Shen, *ACS Nano*, 2018, **12**, 12682-12691.

24. X. Han, Y. Xu, Y. Li, X. Zhao, Y. Zhang, H. Min, Y. Qi, G. J. Anderson, L. You, Y. Zhao and G. Nie,

ACS Nano, 2019, **13**, 4379-4391.

25. K. Yang, H. Xu, L. Cheng, C. Sun, J. Wang and Z. Liu, *Adv Mater*, 2012, **24**, 5586-5592.

26. Y. Jin, X. Yang and J. Tian, *Nanoscale*, 2018, **10**, 9594-9601.

27. Y. Tian, J. Zhang, S. Tang, L. Zhou and W. Yang, *Small*, 2016, **12**, 721-726.

28. N. Jiang, L. Shao and J. Wang, *Adv Mater*, 2014, **26**, 3282-3289.

29. C. Korupalli, C. C. Huang, W. C. Lin, W. Y. Pan, P. Y. Lin, W. L. Wan, M. J. Li, Y. Chang and H. W. Sung, *Biomaterials*, 2017, **116**, 1-9.

30. J. Wang, X. Tan, X. Pang, L. Liu, F. Tan and N. Li, *ACS Appl Mater Inter*, 2016, **8**, 24331-24338.

31. Y. Bai, J. Zhang and X. Chen, *ACS Appl Mater Inter*, 2018, **10**, 14017-14025.

32. X. Tan, J. Wang, X. Pang, L. Liu, Q. Sun, Q. You, F. Tan and N. Li, *ACS Appl Mater Inter*, 2016, **8**, 34991-35003.

33. Y. Ding, S. Su, R. Zhang, L. Shao, Y. Zhang, B. Wang, Y. Li, L. Chen, Q. Yu, Y. Wu and G. Nie, *Biomaterials*, 2017, **113**, 243-252.

34. Y. Xing, T. Ding, Z. Wang, L. Wang, H. Guan, J. Tang, D. Mo and J. Zhang, *ACS Appl Mater Inter*, 2019, **11**, 13945-13953.

35. J. X. Fan, D. W. Zheng, W. W. Mei, S. Chen, S. Y. Chen, S. X. Cheng and X. Z. Zhang, *Small*, 2017, **13**, UNSP 1702714

36. Z. H. Miao, K. Li, P. Y. Liu, Z. Li, H. Yang, Q. Zhao, M. Chang, Q. Yang, L. Zhen and C. Y. Xu, *Adv Healthc Mater*, 2018, **7**, e1701202.

37. X. R. Song, S. H. Li, J. Dai, L. Song, G. Huang, R. Lin, J. Li, G. Liu and H. H. Yang, *Small*, 2017, **13**, UNSP 1603997.

38. G. Zhao, H. Wu, R. Feng, D. Wang, P. Xu, P. Jiang, K. Yang, H. Wang, Z. Guo and Q. Chen, *ACS Appl Mater Inter*, 2018, **10**, 3295-3304.

39. J. Bai, X. D. Jia, Z. F. Ma, X. E. Jiang and X. P. Sun, *Nanoscale*, 2016, **8**, 5260-5267.

40. T. Liu, M. Zhang, W. Liu, X. Zeng, X. Song, X. Yang, X. Zhang and J. Feng, *ACS Nano*, 2018, **12**, 3917-3927.

41. C. Xu, Y. Wang, H. Yu, H. Tian and X. Chen, *ACS Nano*, 2018, **12**, 8255-8265.

42. L. A. Abdulkhaleq, M. A. Assi, M. H. M. Noor, R. Abdullah, M. Z. Saad and Y. H. Taufiq-Yap, *Vet World*, 2017, **10**, 869-872.

43. A. Jiang, Y. Liu, L. Ma, F. Mao, L. Liu, X. Zhai and J. Zhou, *ACS Appl Mater Inter*, 2019, **11**, 6820-6828.

44. C. Zhang, D. F. Hu, J. W. Xu, M. Q. Ma, H. Xing, K. Yao, J. Ji and Z. K. Xu, *ACS Nano*, 2018, **12**, 12347-12356.

45. Y. Wang, Z. Wang, C. Xu, H. Tian and X. Chen, *Biomaterials*, 2019, **197**, 284-293.

46. B. Li, Y. Wang and J. He, *ACS Appl Mater Inter*, 2019, **11**, 7800-7811.

47. M. X. Wu, H. J. Yan, J. Gao, Y. Cheng, J. Yang, J. R. Wu, B. J. Gong, H. Y. Zhang and Y. W. Yang, *ACS Appl Mater Inter*, 2018, **10**, 34655-34663.

48. K. Ke, W. Yang, X. Xie, R. Liu, L. L. Wang, W. W. Lin, G. Huang, C. H. Lu and H. H. Yang, *Theranostics*, 2017, **7**, 4763-4776.

49. T. Guo, Y. Lin, G. Jin, R. Weng, J. Song, X. Liu, G. Huang, L. Hou and H. Yang, *Chem Commun (Camb)*, 2019, **55**, 850-853.

50. A. H. Behzadi, Y. Zhao, Z. Farooq and M. R. Prince, *Radiology*, 2018, **286**, 471-482.

51. L. R. Qiu, D. J. Fernandes, K. U. Szulc-Lerch, J. Dazai, B. J. Nieman, D. H. Turnbull, J. A. Foster, M. R. Palmert and J. P. Lerch, *Nat Commun*, 2018, **9**, 2615.

52.	P. Mi, D. Kokuryo, H. Cabral, H. Wu, Y. Terada, T. Saga, I. Aoki, N. Nishiyama and K. Kataoka, *Nat Nanotechnol*, 2016, **11**, 724-730.

53.	E. M. Gale, H. Y. Wey, I. Ramsay, Y. F. Yen, D. E. Sosnovik and P. Caravan, *Radiology*, 2018, **286**, 865-872.

54.	A. Barandov, B. B. Bartelle, C. G. Williamson, E. S. Loucks, S. J. Lippard and A. Jasanoff, *Nat Commun*, 2019, **10**, 897.

55.	J. Tang, Y. Sheng, H. Hu and Y. Shen, *Progress in Polymer Science*, 2013, **38**, 462-502.
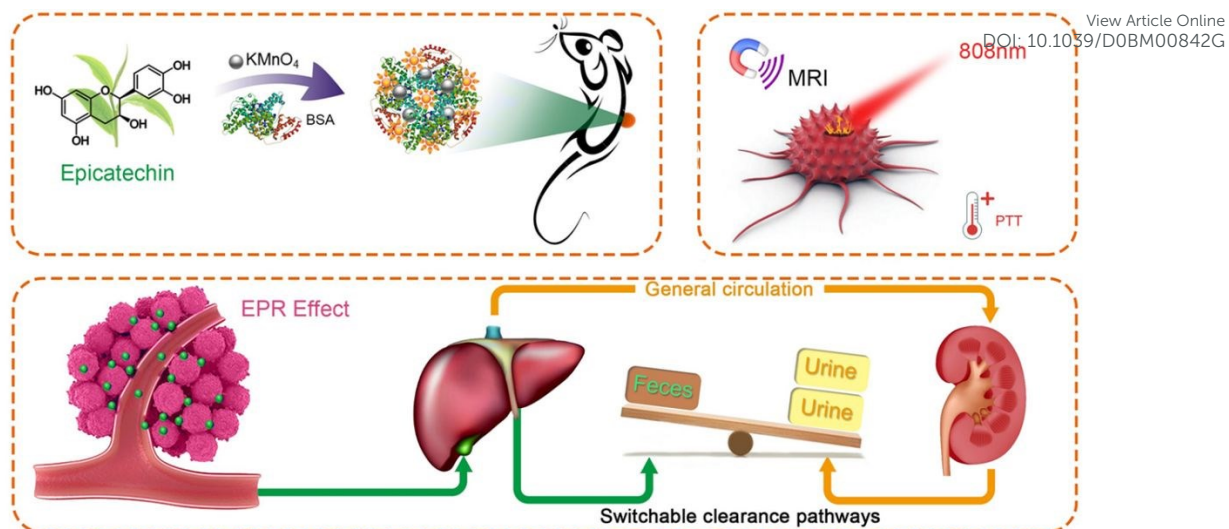
Renal-clearable polyphenol/MnO$_2$ hybrid theranostic agents for multifunctional MRI and photothermal therapy (PTT) *in vivo*.